Nonadiabatic H-Atom Scattering Channels on Ge(111) Elucidated by the Hierarchical Equations of Motion

Xiaohan Dan,[1] Zhuoran Long,[1] Tianyin Qiu,[1] Jan Paul Menzel,[1] Qiang Shi,[2, a)] and Victor Batista[1, 3, b)]

[1)] *Department of Chemistry, Yale University, New Haven, CT 06520, USA*

[2)] *Beijing National Laboratory for Molecular Sciences, State Key Laboratory for Structural Chemistry of Unstable and Stable Species, CAS Research/Education Center for Excellence in Molecular Sciences, Institute of Chemistry, Chinese Academy of Sciences, Zhongguancun, Beijing 100190, China, and University of Chinese Academy of Sciences, Beijing 100049, China*

[3)] *Yale Quantum Institute, Yale University, New Haven, CT 06511, USA*

Atomic and molecular scattering at semiconductor interfaces plays a central role in surface chemistry and catalysis, yet predictive simulations remain challenging due to strong nonadiabatic effects causing the breakdown of the Born–Oppenheimer approximation. Here, we present fully quantum simulations of H-atom scattering from the Ge(111)c(2×8) rest site using the hierarchical equations of motion (HEOM) with matrix product states (MPS). The system is modeled by mapping a density functional theory (DFT) potential energy surface onto a Newns–Anderson Hamiltonian. Our simulations reproduce the experimentally observed bimodal kinetic energy distributions, capturing both elastic and energy-loss channels. By systematically examining atom–surface coupling, incident energy, and isotope substitution, we identify the strong-coupling regime required to recover the experimental energy-loss profile. This regime suppresses the elastic peak, implying additional site-specific scattering channels in the observed elastic peak. Deuterium substitution further produces a subtle shift in the energy-loss peak, consistent with experiment. These results establish HEOM as a rigorous framework for quantum surface scattering, capable of capturing nonadiabatic dynamics beyond electronic friction and perturbative approaches.

[a)]Electronic mail: qshi@iccas.ac.cn

[b)]Electronic mail: victor.batista@yale.edu

I. INTRODUCTION

The Born–Oppenheimer approximation (BOA)[1] is a cornerstone of modern quantum chemistry. It assumes a separation of nuclear and electronic motion, with nuclei evolving on a potential energy surface determined by the electrons. The BOA has been so successful that it is often regarded as a paradigm of molecular science. Despite its success, the BOA breaks down in many important scenarios, including nonadiabatic transitions at conical intersections,[2,3] polaron formation in solids,[4–6] and ultrafast photoinduced dynamics in chemical and biological systems.[7–12] Another critical case arises in molecular interactions with solid surfaces, where the dense manifold of surface electronic states necessitates explicit treatment of electronic excitations in nuclear dynamics. Since such processes are central to heterogeneous catalysis, understanding them is essential for advancing chemical theory and optimizing catalytic processes.[13]

Scattering experiments provide a direct quantification of the interactions of atoms and molecules with solid surfaces. The simplest atom, H atom, has already revealed numerous nonadiabatic effects beyond the BOA in scattering experiments with metal surfaces.[14–17] While momentum and energy conservation predict that in a binary elastic collision with a much heavier atom an H atom would rebound with nearly its initial velocity——valid for insulating surfaces——scattering from a clean Au(111) surface shows pronounced translational energy loss.[15] This loss originates from electron transfer and the creation of electron–hole pairs in the metal, which carry away energy from the scattered atom.

These observations of scattering experiments can be explained by the electronic friction theory, which approximates the effect of surface excitations as frictional and stochastic forces acting on nuclei.[13,16,18–23] Within this framework, nuclei evolve on the adiabatic BOA surface, while nonadiabatic effects enter perturbatively. The electronic friction theory provides an explicit expression for the friction coefficient, which can be computed using *ab initio* methods. For H-atom scattering from Au(111), the local density friction approximation (LDFA)[24] combined with Langevin molecular dynamics successfully reproduced experimental energy-loss distributions.[15]

However, electronic friction has been found to be valid only when nonadiabatic effects primarily involve low-energy excitations. In this perturbative regime, deviations from BOA are modest. When high-energy excitations dominate, the theory fails to make reliable

predictions.[14,25–28] This failure is more pronounced on semiconductors, where electron–hole pair excitations require energies above the band gap. In particular, Krüger et al.[27,29] observed bimodal energy-loss distributions in H-atom scattering from Ge(111)c(2×8), revealing two distinct channels. One channel reflected adiabatic dynamics well described by BOA molecular dynamics, while the second exhibited an energy-loss onset at the Ge band gap. In contrast, the electronic friction theory predicted only one single peak between the two experimental peaks, and failed to capture the correct onset of energy loss at the gap energy.

Recent theoretical studies have provided further insights. Zhu et al.[30] combined density functional theory (DFT) with time-dependent nonadiabatic molecular dynamics (NAMD), showing that nonadiabatic electronic transitions are site-specific and occur selectively at rest sites within a specific spin manifold, although the single-electron treatment limits quantitative comparison with experiment. Lu et al.[31] examined independent electron surface hopping (IESH) and Ehrenfest dynamics, finding that Ehrenfest incorrectly predicts energy loss even for incident energies below the band gap, whereas IESH correctly enforces the gap threshold, with the minimum energy loss equal to the band gap, but the resulting energy-loss profiles increasingly deviate from experiment at higher incident energies.

Here, we employ the hierarchical equations of motion (HEOM) method[32–35] to investigate the scattering dynamics of the H atom on Ge(111)c(2×8) surfaces. HEOM is a non-perturbative, numerically exact framework for open quantum systems that has been widely applied to molecular–metal problems.[36–43] Unlike approximate approaches such as electronic friction theory, HEOM rigorously accounts for atom–surface interactions and captures strong nonadiabatic effects. Its high computational cost, however, has historically limited its application to realistic systems.

Two recent advances have enabled the application of HEOM to simulate scattering dynamics on semiconductor surfaces. First, with the remarkable success of tensor network techniques in representing high-dimensional quantum states, matrix product state (MPS) representations have been introduced into HEOM,[44–47] greatly improving its computational efficiency and enabling applications to more complex scenarios. In particular, the recently developed `mpsqd` package by Guan et al.[46] provides an efficient and user-friendly implementation of MPS-HEOM, substantially facilitating practical simulations. More recently, Preston et al.[43] used MPS-HEOM to investigate vibrational energy relaxation in NO scattering from the Au(111) surface, another system where strong nonadiabatic effects render electronic fric-

tion theory inadequate. Zhang et al.[47] further developed a multiset MPS-HEOM approach to provide a more detailed study on the effect of molecule-metal coupling strength, and compared with the scattering of NO from the Ag(111) surface.

Second, HEOM decomposes environmental interactions into a finite set of effective modes, and the computational cost scales exponentially with the number of effective modes. Traditionally, this has limited HEOM to relatively simple environmental structures. For semiconductors, the complex band structures pose additional challenges for such decompositions. Significant efforts have been made to reduce the number of effective modes. Recently, our group introduced the barycentric spectrum decomposition (BSD) method,[48,49] which employs the adaptive Antoulas–Anderson (AAA) algorithm[50,51] based on barycentric rational representation to the decomposition of effective modes. BSD has been shown to handle fermionic reservoirs effectively and is applicable to, in principle, arbitrary band structures.[49,52]

In this work, we adopt a Newns–Anderson Hamiltonian to describe H-atom scattering on Ge(111), treating both nuclear motion and surface electronic degrees of freedom quantum mechanically. Motivated by experimental and theoretical evidence,[29,30] we focus on the Ge(111) rest site, where nonadiabatic electronic transitions are most likely to occur. This choice captures the dominant scattering pathway while keeping the HEOM simulations tractable.

The one-dimensional potential energy surface (PES) for the Ge(111) rest site is obtained from DFT calculations and fitted to the adiabatic PES of the Newns–Anderson model to determine the model parameters. The resulting Hamiltonian is solved using the MPS-HEOM approach, enabling a fully quantum investigation of how the scattering dynamics depend on atom—surface coupling strength, incident energy, and isotope substitution.

Our simulations reveal that realistic scattering occurs in the strong-coupling regime, where the energy-loss channel closely matches experimental observations. The results further support the interpretation that the two observed scattering channels originate from collisions at different surface sites, consistent with the experimentally proposed site-specific mechanism. In addition, isotope substitution produces a systematic shift of the deuterium energy-loss peak toward higher energy, consistent with the experimental result.

The remainder of this paper is organized as follows. Section II outlines the theoretical framework, including the Newns–Anderson model and the HEOM methodology. Section III

describes the computational setup, where the adiabatic PES is fitted to DFT results to determine model parameters and define the initial kinetic energy distributions. Section IV presents the scattering dynamics and examines the effects of atom–surface coupling strength, incident energy, and isotope substitution. Section V compares our simulations with previous experimental observations and provides additional physical insight. Finally, Section VI summarizes the conclusions of this work.

II. THEORY

A. Newns–Anderson Model

As in many previous studies,[18,53–58] we employ a Newns–Anderson type Hamiltonian to describe the interaction of a hydrogen atom (the "system") with the continuum of electronic states of the Ge(111)c(2×8) surface (the "bath"). The total Hamiltonian is given by (with $\hbar = 1$ throughout):

$$H = \frac{\mathbf{p}^2}{2M} + U_0(\mathbf{x})\hat{c}_H^\dagger \hat{c}_H + U_a(\mathbf{x})\left(1 - \hat{c}_H^\dagger \hat{c}_H\right) + \sum_n \epsilon_n \hat{c}_n^\dagger \hat{c}_n + \sum_n g(\mathbf{x})\left(V_n \hat{c}_n^\dagger \hat{c}_H + V_n^* \hat{c}_H^\dagger \hat{c}_n\right) \ , \quad (1)$$

where $\hat{c}_H^\dagger$ and $\hat{c}_H$ are the creation and annihilation operators of the H atom electronic state, while $\hat{c}_n^\dagger$ and $\hat{c}_n$ correspond to the surface electronic state $|n\rangle$ with energy ϵ_n. The H atom nuclear degrees of freedom are described by momentum $\mathbf{p}$, coordinate $\mathbf{x}$, and mass M.

$U_0(\mathbf{x})$ and $U_a(\mathbf{x})$ denote the diabatic potential energy surfaces (PESs) governing nuclear motion of the H atom. $U_0(\mathbf{x})$ corresponds to the ground state ($|0\rangle$ state) of the neutral H atom, whereas $U_a(\mathbf{x})$ represents the state after electron transfer between the H atom and the Ge surface ($|a\rangle$ state). We choose $|a\rangle$ as the H cation state (so that $\hat{c}_H^\dagger |a\rangle = |0\rangle$), consistent with reports that when H atoms adsorb on the rest atom of the Ge surface, the H atom loses its electron.[30,59,60] The function $g(\mathbf{x})$ accounts for the position-dependent H–surface interaction, and V_n denotes the coupling constant between the surface continuum electronic state $|n\rangle$ and the H atom electronic state.

The system–bath coupling is characterized by the hybridization function,

$$\Gamma(\epsilon) = 2\pi \sum_n |V_n|^2 \, \delta(\epsilon - \epsilon_n) \ , \quad (2)$$

which encodes the interaction between the H atom and the Ge surface electronic continuum.

B. Adiabatic Potential Energy Surface

To obtain a physically meaningful parameterization of the Newns–Anderson model, we fit its adiabatic potential energy surface (PES) to density functional theory (DFT) results. In our previous work,[61] we developed a method to compute the adiabatic potential energy surfaces of the Newns–Anderson model based on the Hellmann–Feynman theorem. The key steps are summarized below.

First, fixing the nuclear position $\mathbf{x}$, the electronic Hamiltonian of Eq. (1) reduces to

$$H_e(\mathbf{x}) = U_a(\mathbf{x}) + \big[U_0(\mathbf{x}) - U_a(\mathbf{x})\big]\hat{c}_H^\dagger \hat{c}_H + \sum_n \epsilon_n \hat{c}_n^\dagger \hat{c}_n + \sum_n \Big(V_n(\mathbf{x})\hat{c}_n^\dagger \hat{c}_H + V_n^*(\mathbf{x})\hat{c}_H^\dagger \hat{c}_n\Big) \ , \quad (3)$$

where $V_n(\mathbf{x}) = g(\mathbf{x})V_n$. This corresponds to a resonant-level model (RLM) with a hybridization function

$$\Gamma(\epsilon, \mathbf{x}) = g^2(\mathbf{x})\,\Gamma(\epsilon) \ , \quad (4)$$

which can be solved exactly using the Green's function formalism.[62,63]

The retarded Green's function is defined as[63,64]

$$\begin{aligned} G^r(\epsilon, \mathbf{x}) &= \Big[\epsilon - \epsilon_H - \Sigma^r(\epsilon, \mathbf{x})\Big]^{-1}, \\ \Sigma^r(\epsilon, \mathbf{x}) &= \int \frac{d\epsilon'}{2\pi} \frac{\Gamma(\epsilon', \mathbf{x})}{\epsilon - \epsilon' + i0^+} \ , \end{aligned} \quad (5)$$

where $\epsilon_H = U_0(\mathbf{x}) - U_a(\mathbf{x})$ and $\Sigma^r(\epsilon, \mathbf{x})$ is the electronic self-energy.

With $G^r(\epsilon, \mathbf{x})$ obtained, the H-state occupation

$$\langle n_H \rangle(\mathbf{x}) = \langle \hat{c}_H^\dagger \hat{c}_H \rangle \quad (6)$$

and the interaction energy

$$\langle H_{\text{int}} \rangle(\mathbf{x}) = \Big\langle \sum_n \big(V_n(\mathbf{x})\hat{c}_n^\dagger \hat{c}_H + V_n^*(\mathbf{x})\hat{c}_H^\dagger \hat{c}_n\big) \Big\rangle \quad (7)$$

can be expressed as[55,61–63,65]

$$\begin{aligned} \langle n_H \rangle(\mathbf{x}) &= -\frac{1}{\pi} \int_{-\infty}^{\infty} d\epsilon\, f(\epsilon)\, \text{Im}[G^r(\epsilon, \mathbf{x})], \\ \langle H_{\text{int}} \rangle(\mathbf{x}) &= -\frac{2}{\pi} \int_{-\infty}^{\infty} d\epsilon\, f(\epsilon)\, \text{Im}[G^r(\epsilon, \mathbf{x})\, \Sigma^r(\epsilon, \mathbf{x})] \ , \end{aligned} \quad (8)$$

where $\text{Im}[\cdot]$ denotes the imaginary part and $f(\epsilon) = [1 + e^{\beta(\epsilon-\mu)}]^{-1}$ is the Fermi–Dirac distribution with $\beta = 1/k_B T$ and chemical potential μ.

The free energy of $H_e(\mathbf{x})$ in the grand canonical ensemble is defined as

$$\mathcal{G}(\mathbf{x}) = -k_B T \ln \Xi(\mathbf{x}), \qquad \Xi(\mathbf{x}) = \mathrm{Tr}\, e^{-\beta(H_e(\mathbf{x})-\mu\hat{N})}. \tag{9}$$

Using the procedure in Ref. 61, the free energy can be expressed as

$$\mathcal{G}(\mathbf{x}) = U_a(\mathbf{x}) - U_a(\mathbf{x}_{\mathrm{ref}}) + \int_{\mathbf{x}_{\mathrm{ref}}}^{\mathbf{x}} d\mathbf{x}' \left\{ \frac{\partial[U_0(\mathbf{x}') - U_a(\mathbf{x}')]}{\partial \mathbf{x}'} \langle n_H \rangle(\mathbf{x}') + \frac{1}{g(\mathbf{x}')} \frac{\partial g(\mathbf{x}')}{\partial \mathbf{x}'} \langle H_{\mathrm{int}} \rangle(\mathbf{x}') \right\}, \tag{10}$$

where $\mathbf{x}_{\mathrm{ref}}$ is a reference position far from the surface.

At zero temperature, the free energy $\mathcal{G}(\mathbf{x})$ reduces to the adiabatic potential energy surface of $H_e(\mathbf{x})$. We therefore denote

$$E_{\mathrm{adia}}(\mathbf{x}) \equiv \mathcal{G}(\mathbf{x})\big|_{T=0} \,, \tag{11}$$

as the adiabatic PES of the Newns–Anderson model.

C. HEOM in the MPS Framework

The Newns–Anderson Hamiltonian in Eq. (1) describes an open quantum system, where the H atom (system) interacts with a fermionic environment consisting of the continuum of electronic states in the semiconductor surface. The dynamics can, in principle, be solved exactly using the HEOM method.[35,66,67]

For semiconductors, however, the complex band structure makes traditional HEOM implementations prohibitively expensive. Shi *et al.*[44] demonstrated that tensor network methods, in particular matrix product states (MPS), provide a highly efficient representation of HEOM, significantly reducing computational cost and extending its applicability. Here, we describe the bath decomposition, HEOM formalism, and MPS representation for MPS-HEOM propagation.

1. Bath Decomposition

Within HEOM, the effect of the electronic continuum is encoded in a set of effective modes obtained by decomposing the bath correlation function into a sum of exponentials:

$$C^{\sigma}(t) = \int_{-\infty}^{+\infty} \frac{d\epsilon}{2\pi}\, e^{\sigma i \epsilon t}\, \Gamma(\epsilon)\, f^{\sigma}(\epsilon) \simeq \sum_{k=1}^{K} d_k^{\sigma}\, e^{-\nu_k^{\sigma} t} \,, \tag{12}$$

where $\sigma \in \{+,-\}$ distinguishes electrons (+) and holes (−), $f^\sigma(\epsilon) = [1 + e^{\sigma\beta(\epsilon-\mu)}]^{-1}$ is the Fermi distribution, and $\Gamma(\epsilon)$ is the hybridization function. The coefficients d_k^σ and frequencies ν_k^σ define the effective modes. The decomposition of $C^\sigma(t)$ for semiconductor-like $\Gamma(\epsilon)$ is performed using the recently developed BSD method.[49]

2. HEOM Formalism

After decomposition, the system coupled to an infinite bath is reformulated as a system interacting with a finite set of effective modes. The density operator $\hat{\rho}_{\mathbf{J}}$ is defined in the composite space

$$\hat{\rho}_{\mathbf{J}} \in \mathcal{F}_e \otimes \mathcal{F}_e^* \otimes \mathcal{H}_x \otimes \mathcal{H}_x^* \otimes \mathcal{F}_{\text{eff}}, \tag{13}$$

where $\mathcal{F}_e$ and $\mathcal{F}_e^*$ are the electronic Fock space of the H atom and its dual ($|0\rangle$ and $|a\rangle$), $\mathcal{H}_x$ and $\mathcal{H}_x^*$ are the nuclear coordinate space of the H atom and its dual, and $\mathcal{F}_{\text{eff}} = \{\mathbf{J}\}$ contains all possible effective mode configurations, where each $\mathbf{J} = \{j_1 j_2, ..., j_\Omega\}$ represents a specific configuration of occupied effective modes with a given order. Here, each $j = (k, \sigma)$, and the maximum number of occupied modes Ω is $2K$.

The reduced density matrix of the system is $\hat{\rho}_{\mathbf{0}}$, corresponding to the configuration where all effective modes are unoccupied. For the Newns–Anderson model with a position-dependent atom–surface coupling in Eq. (1), the HEOM reads:[41,61,68]

$$\frac{\partial}{\partial t}\hat{\rho}_{\mathbf{J}}(t) = -i[H_{\text{mol}}, \hat{\rho}_{\mathbf{J}}] - \gamma_{\mathbf{J}}\hat{\rho}_{\mathbf{J}} - i\sum_{m=1}^{\Omega}(-1)^{\Omega-m}\mathcal{C}_{j_m}\hat{\rho}_{\mathbf{J}_m^-} - i\sum_{j_{\Omega+1}}\mathcal{A}_{\bar{j}_{\Omega+1}}\hat{\rho}_{\mathbf{J}^+}\,, \tag{14}$$

where $\gamma_{\mathbf{J}} = \sum_{(k,\sigma)\in\mathbf{J}} \nu_k^\sigma$. $\mathbf{J}^+$ denotes $\{j_1 j_2, ..., j_\Omega, j_{\Omega+1}\}$, and $\mathbf{J}_m^-$ denotes $\{j_1, ..., j_{m-1}, j_{m+1}, ..., j_\Omega\}$, $\bar{j} = (k, \bar{\sigma})$ with $\bar{\sigma} = -\sigma$. The molecular Hamiltonian is the system part of Eq. (1):

$$H_{\text{mol}} = \frac{\mathbf{p}^2}{2M} + U_0(\mathbf{x})\hat{c}_H^\dagger\hat{c}_H + U_a(\mathbf{x})\left(1 - \hat{c}_H^\dagger\hat{c}_H\right). \tag{15}$$

The operators $\mathcal{C}_j$ and $\mathcal{A}_j$ act as "creation" and "annihilation" superoperators for the effective modes, coupling $\hat{\rho}_{\mathbf{J}}$ to $\hat{\rho}_{\mathbf{J}_m^-}$ and $\hat{\rho}_{\mathbf{J}^+}$, respectively. Their explicit actions are given by:

$$\mathcal{C}_j\hat{\rho}_{\mathbf{J}} = g(\mathbf{x})d_j\hat{c}_j\hat{\rho}_{\mathbf{J}} - (-1)^\Omega d_{\bar{j}}^*\hat{\rho}_{\mathbf{J}}\hat{c}_j g(\mathbf{x}), \tag{16a}$$

$$\mathcal{A}_j\hat{\rho}_{\mathbf{J}} = g(\mathbf{x})\hat{c}_j\hat{\rho}_{\mathbf{J}} + (-1)^\Omega\hat{\rho}_{\mathbf{J}}\hat{c}_j g(\mathbf{x}). \tag{16b}$$

For $j = (k, \sigma)$, we have $d_j = d_k^\sigma$, and $\hat{c}_j = \hat{c}_H^\sigma$ where $\hat{c}_H^{-(+)} \equiv \hat{c}_H^{(\dagger)}$ denotes the system annihilation (creation) operators.

3. *MPS Representation*

In practice, the large hierarchy of all density operators $\hat{\rho}_{\mathbf{J}}$ is represented compactly using the MPS ansatz:[44,46]

$$\hat{\rho}_{\mathbf{J}} \approx \sum_{\alpha_1=1}^{r_1} \cdots \sum_{\alpha_{d-1}=1}^{r_{d-1}} A_1(n_1, \alpha_1) A_2(\alpha_1, n_2, \alpha_2) \cdots A_d(\alpha_{d-1}, n_d), \tag{17}$$

here, A_i are three-dimensional tensors, except that the first and last tensors are two-dimensional. $r_i\,(i = 1, ..., d)$ denotes the i-th bond dimension of the MPS. The total dimension is $d = 2K + 4$, covering all spaces included in Eq. (13). Specifically, the first four tensors correspond to the degrees of freedom for the electronic Fock space, its dual, the nuclear coordinate space of the H atom, and its dual, respectively. The remaining $2K$ tensors correspond to the degrees of freedom in $\mathcal{F}_{\text{eff}}$. In detail, n_1 and n_2 represent the electronic states $\{0, a\}$, while n_3 and n_4 correspond to the nuclear coordinate basis $\{\mathbf{x}\}$. All possible configurations $\mathbf{J}$ in $\mathcal{F}_{\text{eff}}$ are mapped to the occupation number basis $\{n_5, \cdots, n_{2K+4}\}$, where $n_i = 0$ or 1 for $i = 5, ..., 2K + 4$.

Time evolution is performed with the time-dependent variational principle (TDVP),[69] which integrates the dynamics while maintaining a fixed MPS bond dimension. In practice, simulations are performed by systematically increasing the bond dimension to ensure convergence of the dynamics. Further details can be found in Refs. 44 and 46. The TDVP-based HEOM propagation has been implemented in the `mpsqd`[46] package.

III. COMPUTATIONAL SETUP

A. System–Bath Interaction

In this work, the coupling between the H atom and the Ge(111) surface is described by the following hybridization function:

$$\Gamma(\epsilon) = \frac{\eta\gamma^2}{(\epsilon - \epsilon_0)^2 + \gamma^2} \left[1 - \frac{1}{1 + e^{(\epsilon - E_B/2)/\delta}} \frac{1}{1 + e^{-(\epsilon + E_B/2)/\delta}}\right], \tag{18}$$

where $E_B = 0.49$ eV is the Ge(111) band gap,[27] $\delta = 0.02$ eV controls the smoothness of the band edges, $\epsilon_0 = 0$ sets the band center, and $\gamma = 1.5$ eV determines the bandwidth. The overall coupling strength η is treated as a tunable parameter in the range 1–3 eV, reflecting the uncertainty of its precise value for the realistic surface.

Physically, $\Gamma(\epsilon)$ characterizes the energy-dependent interaction strength between the H atom electronic state and the continuum of surface states, thereby determining the probability of charge transfer and energy dissipation into the surface. This hybridization function, together with the Fermi distribution, serves as input for the bath correlation function $C^\sigma(t)$ [Eq. (12)]. The temperature is set to $T = 300$ K, which enters via the Fermi function. To decompose $C^\sigma(t)$ into exponential terms, we employ the BSD scheme,[49] which expands both the hybridization function and the Fermi distribution into a finite set of effective modes.

Figure 1 illustrates the BSD approximations for $\Gamma(\epsilon)$ and the Fermi distribution. The relative error of their product $\Gamma(\epsilon)f^\sigma(\epsilon)$ remains below 10^{-3} across the entire energy range. Such accuracy has been demonstrated to be sufficient for the present type of simulations.[49] In practice, 13 effective modes are obtained: 6 from the hybridization function and 7 from the Fermi distribution.

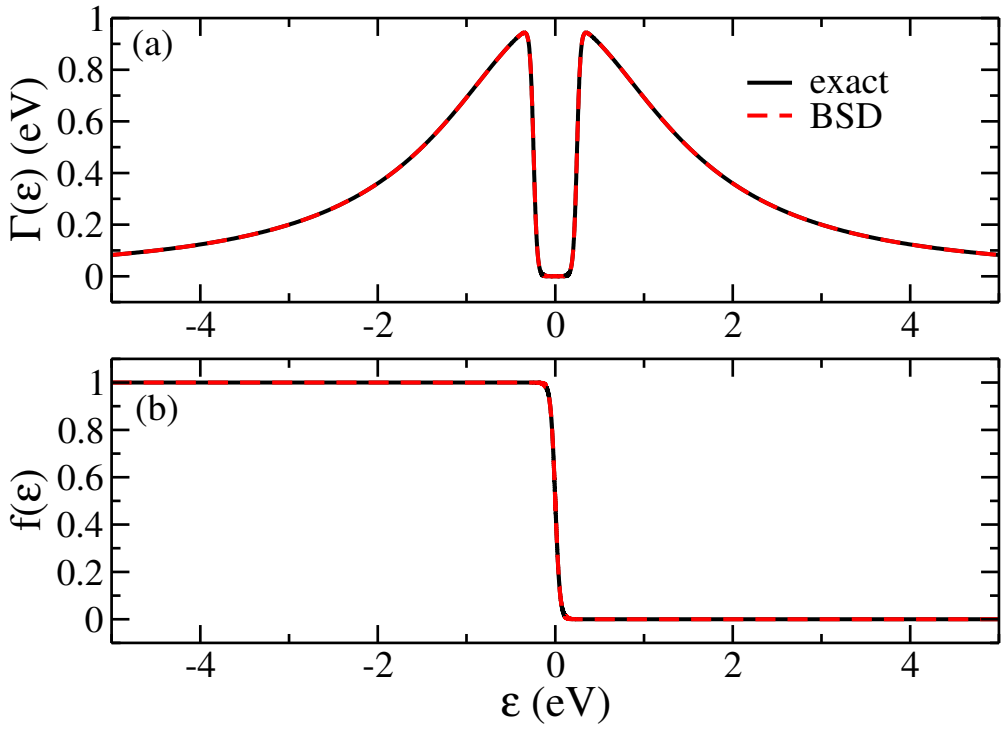

FIG. 1. Accuracy of the BSD approximation for (a) the hybridization function $\Gamma(\epsilon)$ (with $\eta = 1$ eV) and (b) the Fermi distribution at $T = 300$ K. The relative error of their product $\Gamma(\epsilon)f^\sigma(\epsilon)$ is below 10^{-3} across the full energy range.

B. Model Parametrization

The potential energy surface (PES) for H-atom scattering at the Ge(111) rest site was obtained from density functional theory (DFT) calculations using the Vienna *Ab Initio* Simulation Package (VASP) with the projector augmented wave (PAW) method.[70] Calculations were carried out at the PBE level[71] with D3-BJ dispersion corrections.[72,73] A plane-wave cutoff of 450 eV and a Γ-centered $1 \times 3 \times 1$ Monkhorst–Pack k-point grid[74] were employed. The Ge(111) slab[75] was modeled with four atomic layers, with the bottom two layers fixed during geometry optimization.

To reproduce the DFT PES within the Newns–Anderson model, we fit the adiabatic PES using the following analytic forms for $U_0(x)$ and $U_a(x)$:

$$U_0(x) = A_0 \left(e^{2C_0(x-x_0)} - 2e^{C_0(x-x_0)}\right), \tag{19a}$$

$$U_a(x) = A_1 \left(e^{2C_1(x-x_1)} - 2e^{C_1(x-x_1)}\right) + B_1 + \frac{1}{(x-D_1)^4}. \tag{19b}$$

Here, $U_0(x)$ follows the Morse potential form, while $U_a(x)$ includes an additional short-range repulsive term $1/(x-D_1)^4$ to capture the strong repulsion experienced by the H atom near the Ge(111) surface. The constant offset B_1 is fixed at 8.8 eV, corresponding to the difference between the H atom ionization potential (13.6 eV) and the Ge(111) work function (4.8 eV).[76]

The position-dependent interaction between the H atom and the surface is described by a sigmoidal coupling function,

$$g(x) = \frac{2}{1 + e^{-c_g(x-x_g)}}, \tag{20}$$

with x_g and c_g as adjustable parameters.

Using the procedure in Sec. II B, we calculate the adiabatic energy $E_{\text{adia}}(x)$ and occupation number $\langle n_H \rangle(x)$ for a given parameter set. These quantities are then fitted to DFT reference data: the DFT PES and the spin magnetic moment. The resulting optimized parameters are summarized in Table I.

Figure 2(a) shows the model potentials $U_0(x)$, $U_a(x)$, and the coupling function $g(x)$ along with the computed $E_{\text{adia}}(x)$ and the DFT PES. Figure 2(b) compares the calculated occupation number $\langle n_H \rangle(x)$ with the spin magnetic moment obtained from DFT. In both the $E_{\text{adia}}(x)$ and $\langle n_H \rangle(x)$ calculations, we use $\eta = 3$ eV.

Overall, the Newns–Anderson model captures the essential features of the DFT PES and the spin magnetic moment transition. While minor deviations arise from the use of

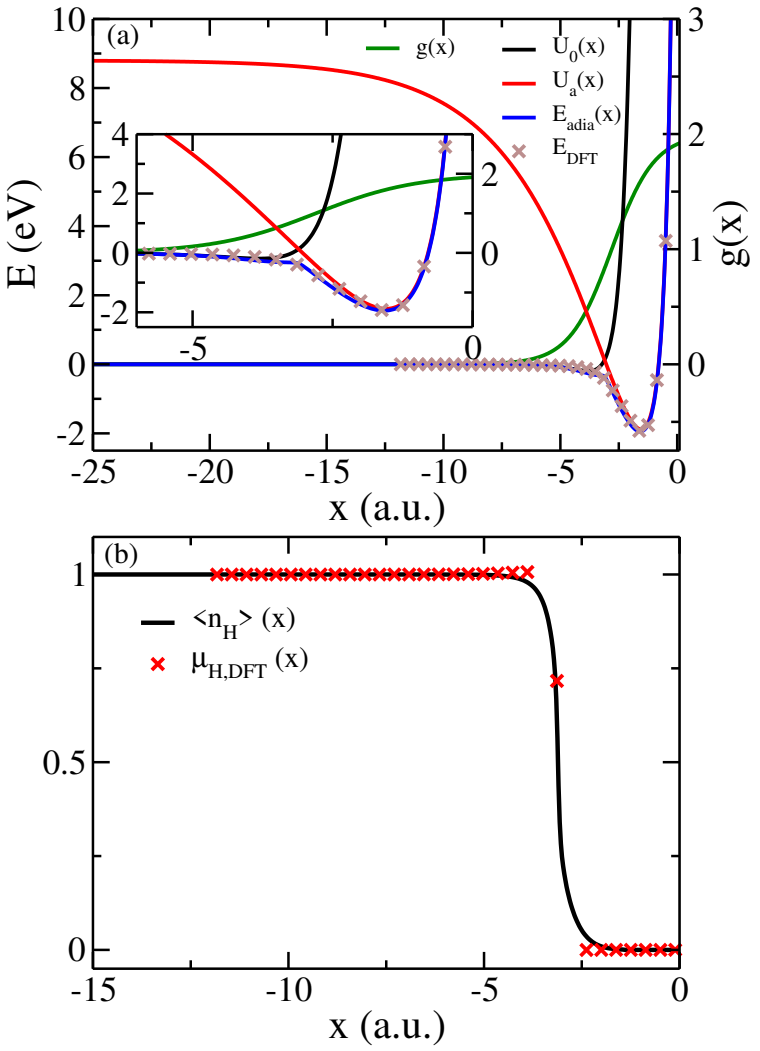

FIG. 2. (a) Model potentials $U_0(x)$, $U_a(x)$, and position-dependent coupling $g(x)$ in the Newns–Anderson model, together with the computed adiabatic energy $E_{\mathrm{adia}}(x)$ and DFT reference E_{DFT}. (b) Calculated occupation number $\langle n_H \rangle(x)$ compared with the spin magnetic moment μ_H from DFT results. All parameters are listed in Table I. For both panels, η is set to 3 eV.

analytical functional forms, our aim is not to reproduce the DFT PES exactly. Rather, the resulting parameter set provides a physically meaningful basis for simulating the scattering dynamics.

C. Kinetic Energy Distribution

The momentum-space distribution at electronic state $|i\rangle$ ($i \in \{0, a\}$) is defined as

$$\rho_{ii}(k) = \frac{1}{2\pi} \int dx \int dx' \, e^{-ik(x-x')} \, \rho_{ii}(x, x'), \tag{21}$$

where $\rho_{ii}(x, x')$ is the reduced coordinate-space density matrix at state i:

$$\rho_{ii}(x, x') \equiv \langle i | \langle x | \, \hat{\rho} \, | x' \rangle \, | i \rangle \, . \tag{22}$$

Here, $\hat{\rho}$ is the reduced density operator (i.e., $\hat{\rho}_{\mathbf{0}}$ in HEOM). In other words, $\rho_{ii}(k)$ corresponds to the diagonal element of the Fourier transform of the coordinate-space reduced density operator.

The kinetic energy distribution at state $|i\rangle$, denoted as $P_i(E)$, is then given by

$$P_i(E) = \rho_{ii}(k) \frac{dk}{dE} = \frac{\rho_{ii}(k)}{\hbar} \sqrt{\frac{M}{2E}}, \tag{23}$$

where we use the relation $E = \hbar^2 k^2 / (2M)$ for the kinetic energy.

As $E \to 0$, $\sqrt{1/E}$ becomes large, resulting in a sharp peak in the numerically obtained $P_i(E)$ at small E values.[61] According to our PES shown in Fig. 2, H atoms with such low kinetic energies cannot escape from the semiconductor surface and remain trapped nearby. In contrast, experimental kinetic energy distributions, measured using time-of-flight techniques,[27] should not include contributions from atoms trapped near the surface.

To enable a direct comparison with experiments, we exclude these trapped components when calculating the kinetic energy distribution. This is achieved by projecting out the near-surface contributions:

$$\hat{\rho}^{\mathrm{pj}} = \mathcal{P} \hat{\rho} \mathcal{P} \quad , \tag{24}$$

where $\hat{\rho}$ is the reduced density operator and $\mathcal{P}$ is a projection operator that removes the distribution near the surface. In this work, we choose the projection operator as

$$\mathcal{P} = I - \sum_{E_i < 0} |\psi_i\rangle\langle\psi_i| \tag{25}$$

where I is the identity operator, $|\psi_i\rangle$ and E_i are the i-th eigenstate and eigenenergy of the adiabatic PES, i.e., $E_{\mathrm{adia}}(x)$ in Eq. (11).

By performing the same procedure as in Eqs. (21)–(23) but using $\hat{\rho}^{\mathrm{pj}}$, we obtain the kinetic energy distribution with the bound state contributions projected out, denoted as $P_i^{\mathrm{pj}}(E)$.

IV. RESULTS

A. H-Atom Scattering Dynamics

In all simulations, the nuclear degree of freedom x is represented using the potential optimized discrete variable representation (PO-DVR).[77,78] Unless otherwise noted, the DVR grid spans $x \in [-60, 0.2]$ a.u. The number of PO-DVR basis functions, up to 1000, depends on the incident kinetic energy, atom–surface coupling strength, and isotope effect. The H atom is initially prepared in the neutral state $|0\rangle$ with a Gaussian wavepacket centered at $x = -11$ a.u. and a spatial width of $\sigma_x = 1$ a.u. In this subsection, we consider an incident energy $E_{\text{in}} = 1.92$ eV and coupling strength $\eta = 3$ eV.

Figure 3 shows the population dynamics of the H atom in states $|0\rangle$ and $|a\rangle$ during the scattering process. At $t \approx 20$ fs, the wavepacket reaches the Ge surface and electron transfer from the H atom to the surface begins, seen as a sharp decrease in $P_0(t)$ accompanied by an increase in $P_a(t)$. By $t \approx 30$ fs, the electron transfer reaches its maximum, with nearly the entire wave packet occupying the $|a\rangle$ state. As the atom rebounds, electrons transfer back to the H atom, driving a transition from $|a\rangle$ to $|0\rangle$. Most of this back-transfer is completed by $t \approx 50$ fs, small oscillations in $P_0(t)$ and $P_a(t)$ after 50 fs reflect residual charge exchange near the surface. After $t > 100$ fs, the population curves stabilize. By the end of the simulation, most of the H atom escapes in the $|0\rangle$ state, while a small fraction remains trapped near the surface in the $|a\rangle$ state.

To further describe the scattering process, we present the evolution of wave packet distributions $P_0(x)$ and $P_a(x)$ in Figure 4. Initially, the wavepacket approaches the Ge surface from the left ($x < 0$). Upon reaching the surface at $t \approx 20$ fs, electron transfer causes $P_0(x)$ to decrease and $P_a(x)$ to rise. By $t \approx 50$ fs, $P_0(x)$ begins to propagate away from the surface and gradually delocalizes, signaling a loss of kinetic energy.

By the end of the simulation, a small peak of $P_0(x)$ remains localized near the surface, reflecting a low-energy component that lacks sufficient kinetic energy to escape. Meanwhile, a portion of $P_a(x)$ persists, oscillating within the well of $U_a(x)$ near the surface, indicating that some H atoms become adsorbed on the Ge surface in the $|a\rangle$ state after scattering. The pronounced oscillatory features of $P_a(x)$ further suggest that this population occupies excited vibrational levels on the $|a\rangle$ state.

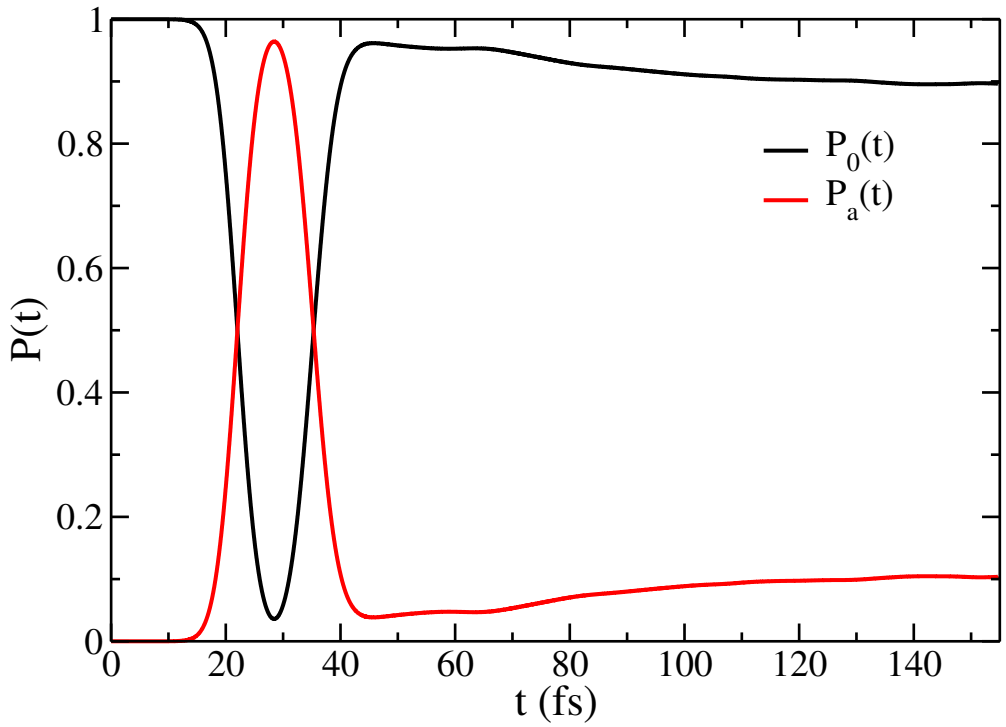

FIG. 3. Time evolution of H-atom populations in states $|0\rangle$ and $|a\rangle$, denoted $P_0(t)$ and $P_a(t)$, respectively, during the scattering process.

To facilitate comparison with experimental results, we plot in Figure 5 the kinetic energy distribution of the H atom in the $|0\rangle$ state (H-neutral) at the time of emission ($t = 154.8$ fs). The projection technique described in Sec. III C is applied to exclude small contributions from wavepackets trapped near the surface. The resulting distribution exhibits a bimodal structure. The dominant peak spans 0–1.5 eV with a maximum near 1 eV, corresponding to the energy-loss channel. Its shape and position agree well with the experimental observations reported by Krüger *et al.*[27] In addition, a much weaker Gaussian-like peak appears near the incident energy 1.92 eV. This peak corresponds to the elastic scattering channel, arising from a small portion of the H wavepacket that scatters without exchanging electrons with the surface. Because of its very small weight, this elastic peak is not discernible in Figure 4. Overall, our simulations capture the bimodal feature observed experimentally. However, the relative ratio of the two channels differ significantly from experiment, which will be discussed later in Sec. V.

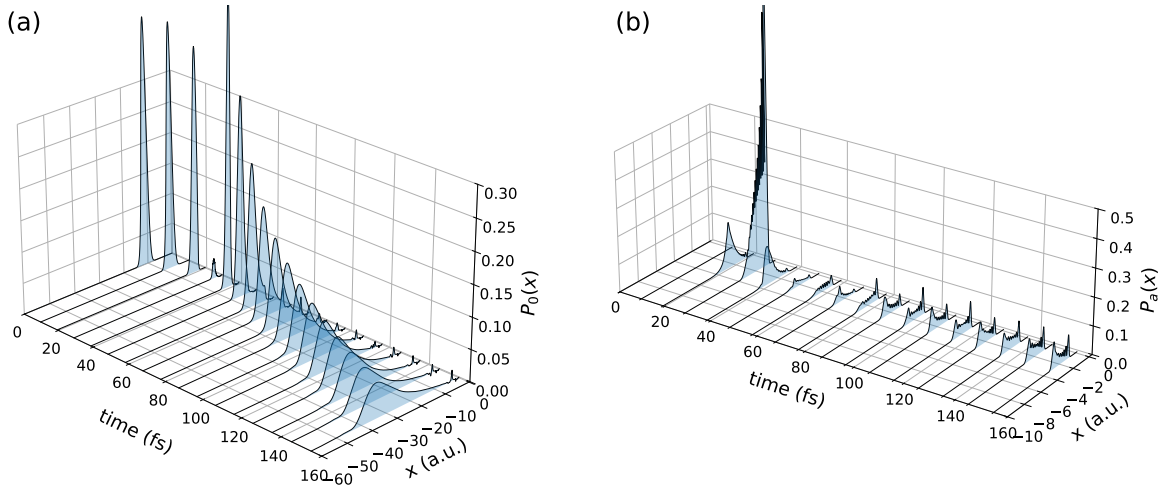

FIG. 4. Spatial probability distributions of the H atom in the $|0\rangle$ and $|a\rangle$ states during the scattering process, denoted as $P_0(x)$ and $P_a(x)$, respectively. Panel (a) shows $P_0(x)$, and Panel (b) shows $P_a(x)$.

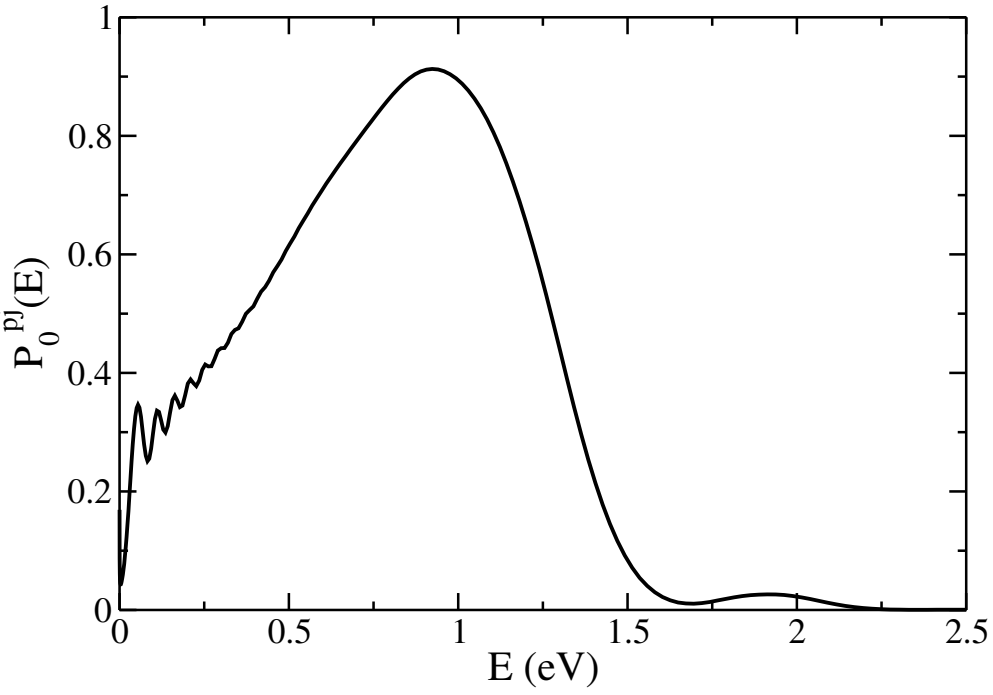

FIG. 5. Kinetic energy distribution of the H atom emitted in the $|0\rangle$ state at $t = 154.8$ fs, projected using the technique in Sec. III C to exclude some near-surface contributions.

The dominant energy-loss peak originates from scattering events involving electronic transitions with the semiconductor, thereby reflecting the band structure characteristics of the material. Consider the following process: an H atom donates an electron to the conduction band of Ge(111), and after the collision, it regains an electron from the valence band. Since the returning electron has lower energy than the donated one, such an electronic transition is expected to result in an energy loss approximately equal to the band gap. This mechanism explains why the high-energy edge of the loss peak lies $E_g = 0.49$ eV below the incident energy.

B. Effects of Atom–Surface Coupling Strength

In the previous simulations, we set the coupling parameter to $\eta = 3$ eV. The present framework allows us to vary η systematically, providing mechanistic insight into how atom–surface coupling influences scattering dynamics. In earlier work,[61] we showed that coupling strength modulates the degree of adiabaticity: weak coupling favors nonadiabatic transitions, while strong coupling yields more adiabatic behavior, where the electronic friction theory becomes applicable. Here, we extend this analysis to H-atom scattering from a semiconductor surface.

Figure 6 shows the time evolution of the neutral-state population $P_0(t)$ for different atom—surface coupling strengths. As η increases, a larger fraction of the wavepacket undergoes electron transfer to the surface, reflected by the reduced $P_0(t)$ around $t \approx 30$ fs. For $\eta > 2$ eV, the transfer probability saturates, with nearly complete electronic excitation during the collision. Stronger coupling also accelerates both the decay and recovery of $P_0(t)$, reflecting faster electron transfer. After scattering, the larger final value of $P_0(t)$ at higher η indicates that more population returns to the neutral state and scatters back, while less remains trapped in the $|a\rangle$ state.

Figure 7 presents the projected kinetic energy distributions of the H atom in the neutral state at $t = 154.8$ fs for various η. At weak coupling, the elastic scattering channel is relatively pronounced, and its relative intensity decreases with increasing η, indicating a higher probability of electronic transitions, consistent with the population dynamics in Figure 6. The energy-loss peak also depends strongly on η: for weak coupling, the peak is broader, decreases in intensity, shifts significantly toward lower energies, and exhibits fine structure.

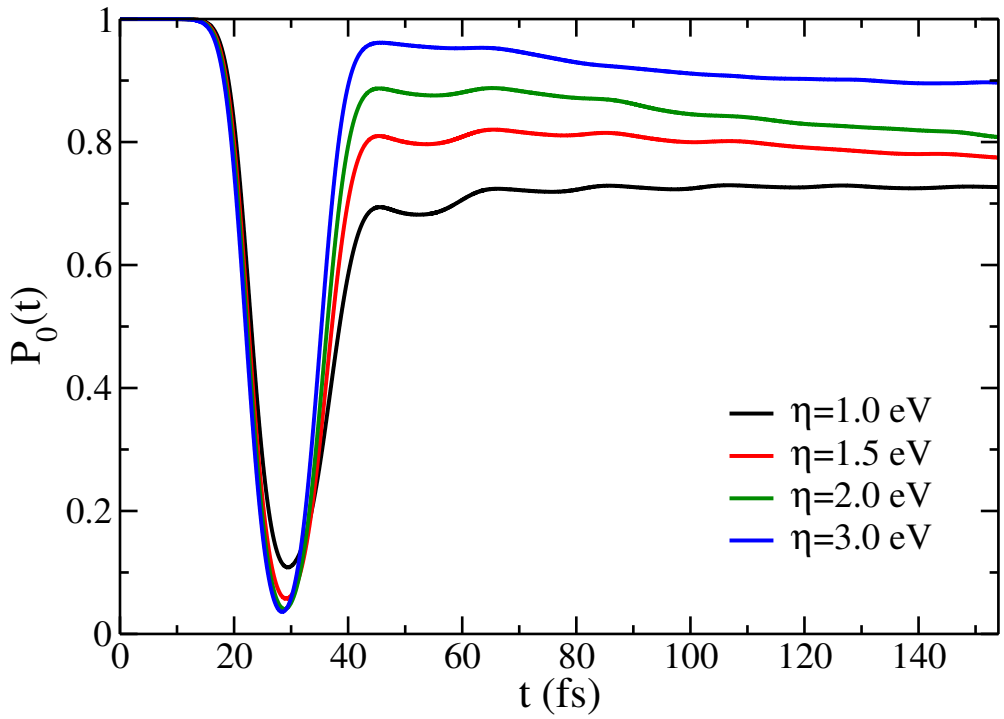

FIG. 6. Time evolution of the H-atom population in the neutral state $|0\rangle$ for different coupling strengths η. The incident energy is $E_{\text{in}} = 1.92$ eV. All other parameters are identical to those in Table I.

These fine structures originate from discrete bound states of the excited potential $U_a(x)$ and higher-order processes such as multiple electron transfers. Specifically, when the H atom is excited to the $|a\rangle$ state, the bound states of $U_a(x)$ are discretely spaced rather than forming a continuum. These distinct excitation pathways can modulate the scattering dynamics, thereby shaping the observed structure in the energy distribution. Such fine structures are gradually washed out as η increases.

The narrowing of the energy-loss peak and its shift toward higher kinetic energies with increasing η indicate enhanced adiabaticity of the dynamics. However, unlike H-atom scattering on metal surfaces, where the high-energy edge of the distribution typically approaches the initial kinetic energy, here the high-energy edge of the energy-loss peak remains around 1.5 eV, roughly one band gap below the initial kinetic energy. Thus, while strong coupling drives the dynamics toward adiabatic behavior, nonadiabatic effects remain intrinsic due to the semiconductor band structure. This persistent band-gap-related energy loss explains why the electronic friction theory fails to capture scattering on semiconductor surfaces.

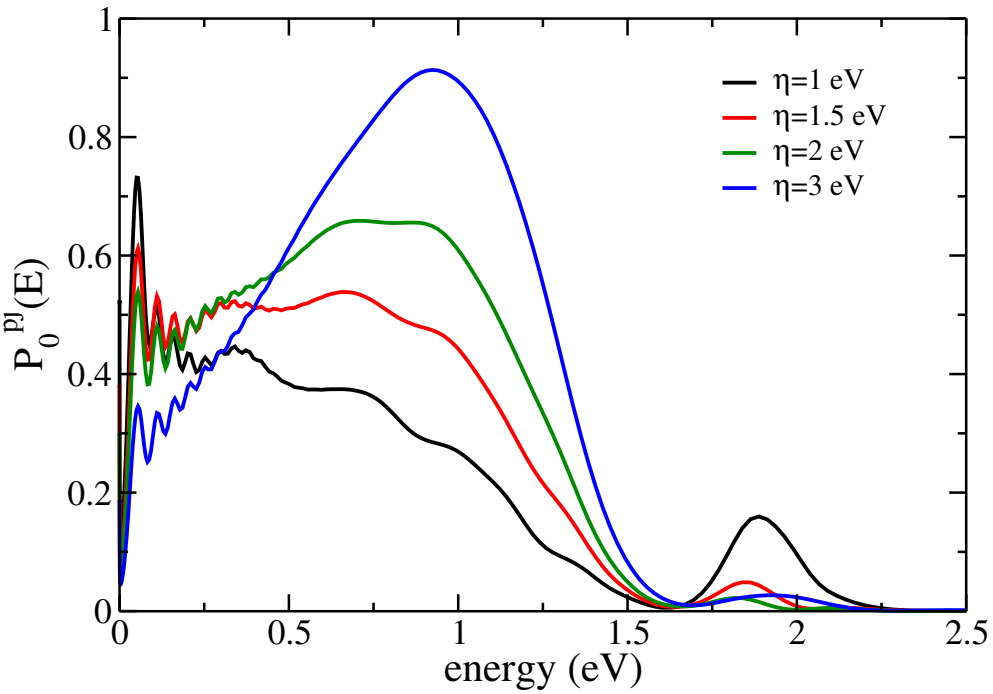

FIG. 7. Projected kinetic energy distributions of H atoms in the neutral state $|0\rangle$ at $t = 154.8$ fs for various coupling strengths η. All other parameters are identical to those in Table I.

C. Effects of Incident Energy

We now examine how the incident kinetic energy E_{in} influences the scattering outcome. Figure 8 shows the projected kinetic energy distributions of the H atom in the neutral state after scattering at different incident energies. Panel (a) corresponds to $\eta = 1$ eV, while panel (b) corresponds to $\eta = 3$ eV. The corresponding times chosen for $E_{in} = 0.37$, 0.99, 1.92, and 6.17 eV are $t = 164.5$, 193.5, 154.8, and 91.9 fs, respectively. For $E_{in} = 0.37$ eV, a smaller box in the range -30 to 0.2 a.u. was employed. In all cases, the outgoing wave packets have propagated well beyond the scattering region.

For weak coupling ($\eta = 1$ eV), the elastic peak persists at all incident energies. The relative weight of the energy-loss channel increases as E_{in} increases. At $E_{\text{in}} = 0.37$ eV (below the band gap), only elastic scattering is observed, with no energy-loss channel. At $E_{\text{in}} = 0.99$ eV, an energy loss feature appears below $E \approx 0.5$ eV, consistent with the Ge band gap. At $E_{\text{in}} = 1.92$ eV, the energy-loss channel becomes more pronounced compared to the $E_{\text{in}} = 0.99$ eV case. In both the $E_{\text{in}} = 0.99$ and 1.92 eV cases, a substantial near-zero-energy component is present, originating from wavepacket components with kinetic energies

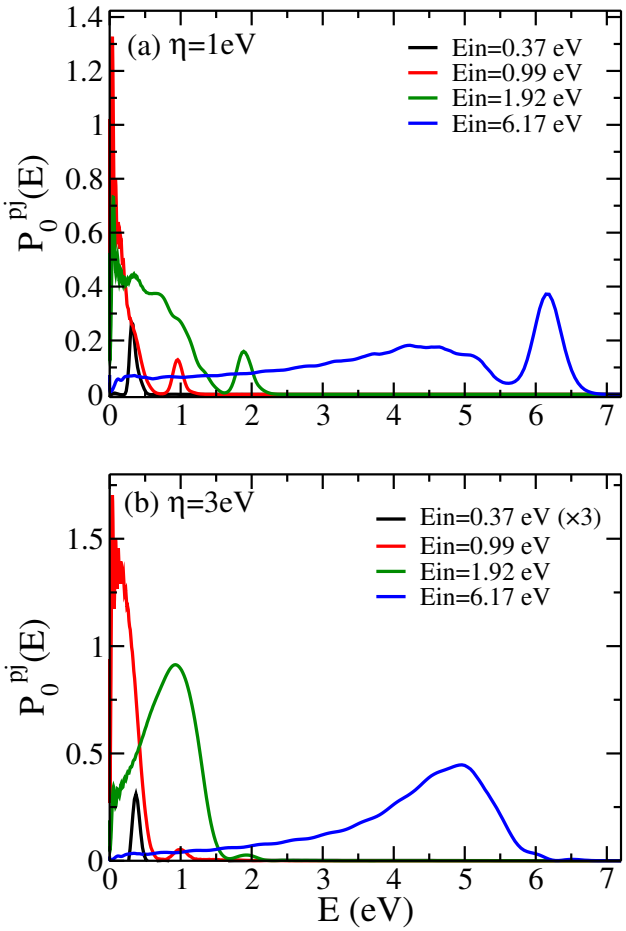

FIG. 8. Projected kinetic energy distributions of the H atom in the $|0\rangle$ state after scattering at different incident energies $E_{\rm in}$. (a) $\eta = 1$ eV. (b) $\eta = 3$ eV. For clarity, the distribution at $E_{in} = 0.37$ eV in panel (b) is scaled by a factor of 3 due to its small magnitude. All distributions were evaluated at sufficiently long times, when the outgoing wavepacket had moved far from the scattering region. All other parameters are identical to those listed in Table I.

insufficient to escape from the surface. At the highest incident energy of 6.17 eV, the distribution in the energy-loss channel rises sharply from $E \approx 5.6$ eV toward lower energies, reaches a maximum, and then gradually decreases. Integration over the energy-loss channel shows that it contains an even larger contribution than that for $E_{\rm in} = 1.92$ eV.

For strong coupling ($\eta = 3$ eV), the elastic scattering peak is significantly suppressed across all incident energies. Note that the distribution at $E_{\rm in} = 0.37$ eV in panel (b) is multiplied by a factor of three for visibility. The energy-loss peak appears only when $E_{\rm in}$ exceeds the band gap, and integration over the distributions confirms that the population in

the energy-loss channel continues to grow with increasing $E_{\rm in}$. Consistent with the discussion in the previous subsection on the effect of atom–surface coupling strength, the profile of the energy-loss channel undergoes substantial changes with increasing η for different E_{in}: the peak becomes smoother, shifts toward higher kinetic energies, and the low-energy component is reduced.

D. Isotope Effect

We now investigate the effect of isotope substitution on the scattering dynamics. Figure 9 shows the projected kinetic energy distributions $P_0^{\rm pj}(E)$ for H and D atoms at two incident energies ($E_{\rm in}$ = 1.92 and 6.17 eV) and for both weak (η = 1 eV) and strong (η = 3 eV) atom–surface coupling. The left and right panels correspond to $E_{\rm in}$ = 1.92 and 6.17 eV, respectively, while the top and bottom panels correspond to η = 1 and 3 eV, respectively. For D-atom simulations, all parameters are kept identical to those for H, except that the mass of D is set to be twice that of H. The distributions are evaluated after the outgoing wavepacket has propagated well beyond the scattering region: t = 154.8 fs for H and t = 222.5 fs for D at $E_{\rm in}$ = 1.92 eV; t = 91.9 fs for H and t = 135.5 fs for D at $E_{\rm in}$ = 6.17 eV.

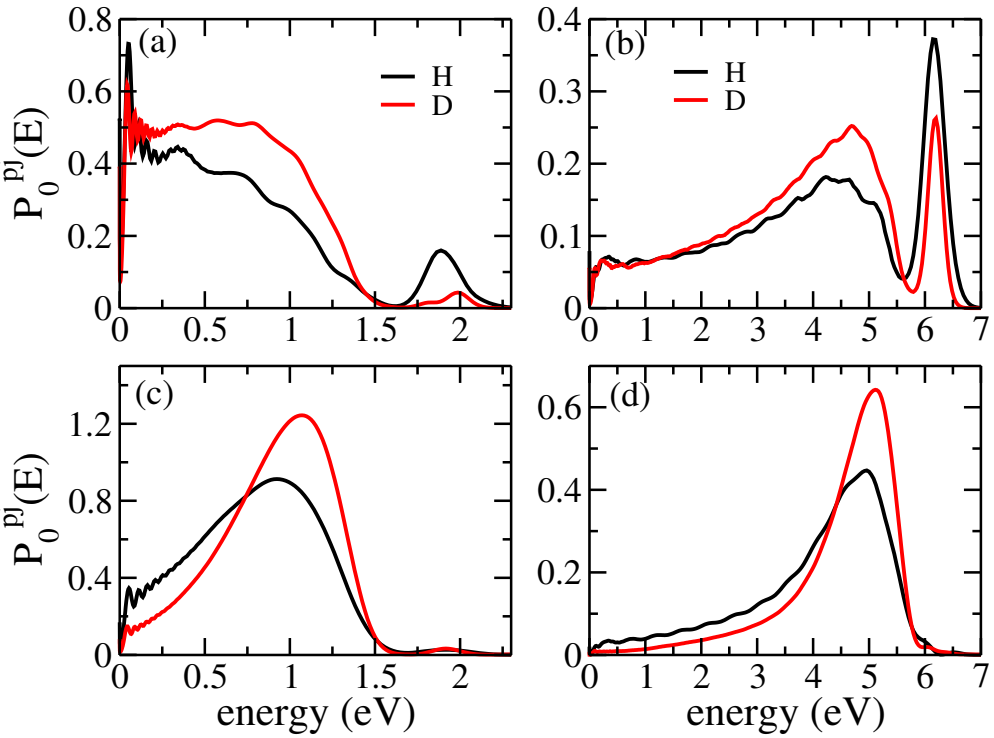

FIG. 9. Projected kinetic energy distributions in the $|0\rangle$ state from scattering simulations of H and D atoms at two incident energies and two coupling strengths. Panels (a)–(d) correspond to (E_{in}, η) = (1.92 eV, 1 eV), (6.17 eV, 1 eV), (1.92 eV, 3 eV), and (6.17 eV, 3 eV), respectively. Distributions are evaluated when the outgoing wavepacket has moved far away from the scattering region for each case.

For weak coupling (η = 1 eV), replacing H with D reduces the elastic scattering peak, enhances the energy-loss channel, and shifts its peak toward higher kinetic energies. For strong coupling (η = 3 eV), where the elastic peak is already small, isotope substitution primarily narrows the energy-loss peak, reduces the low-energy component, and shifts the peak to higher energies. Comparison with Figure 7 indicates that, for different E_{in} and η, replacing H with D consistently produces effects similar to increasing the atom–surface coupling strength.

This trend is physically intuitive. At the same incident energy, the heavier D atom has a lower velocity, thereby increasing the adiabaticity of the scattering process. According to the Landau–Zener formula,[79–81] the probability of a diabatic transition contains an exponential term with a factor $|V_{ab}|^2/v$, where V_{ab} is the nonadiabatic coupling between diabatic states $|a\rangle$ and $|b\rangle$, and v is the velocity. A decrease in v thus has the same effect as an increase in

$|V_{ab}|^2$. In our model, the coupling strength η plays a role analogous to $|V_{ab}|^2$, so the isotope effect observed when replacing H with D mimics the effect of increasing η.

V. DISCUSSION

In this work, we present simulations of H-atom scattering on the Ge(111) surface. Our results show qualitative agreement with recent experimental findings,[27,29] while certain discrepancies remain. Since our calculations employ the HEOM approach to obtain numerically exact solutions within the Newns–Anderson model framework, these deviations are likely due to intrinsic limitations of the model. This section is devoted to a detailed comparison between our theoretical predictions and the recent experimental observations.

A. H-Atom Scattering: Simulation and Experiment

Our calculations predict a bimodal structure in the kinetic energy distribution of the scattered H atom, although the elastic scattering channel in this bimodal structure becomes less pronounced under strong coupling. This behavior originates from the gapped band structure of the semiconductor surface, indicating that the HEOM method provides a reliable nonperturbative description of H-atom scattering on semiconductor surfaces. Since the employed Newns–Anderson model accounts solely for interactions with surface electronic states and neglects surface phonons, this further supports that the bimodal structure arises from valence-to-conduction band excitations, producing high-energy electron–hole pairs.

Experiments have shown that the energy-loss channel is strongly promoted by the incident translational energy.[27] Our results exhibit the same trend: for both $\eta = 1$ eV and $\eta = 3$ eV, the integrated population of the energy-loss channel in Figure 8 increases with increasing incident energy. Analysis of the integrated population further indicates that the outgoing population grows with incident energy, consistent with the experimental observation that sticking probability decreases as the incident energy increases.[27,29]

However, despite capturing this qualitative trend, the simulations do not reproduce the experimentally observed quantitative branching ratio between the elastic and energy-loss channels. We attribute this discrepancy to two factors. First, our model focuses on scattering at the Ge(111) rest site, whereas the experimental branching ratios reflect statistical

averages over multiple surface sites. Second, as shown in Figure 7, the atom–surface coupling parameter η significantly influences the relative weights of the two channels. Yet, as a model parameter, its precise value has not been definitively quantified.

Then, what magnitude of η best corresponds to the actual case? Based on the results in Figs. 7 and 8, we identify $\eta = 3$ eV (strong coupling) as most representative, as the resulting energy-loss channel closely reproduces both the peak position and overall lineshape observed experimentally.[27] This value of η also aligns with previous HEOM simulations of H scattering on Au(111),[61] suggesting a relatively consistent atom–surface coupling across different surfaces.

To further validate this assessment, Figure 10 compares the simulated energy-loss distributions at $\eta = 3$ eV for different incident energies with the experimental data from Fig. 1 of Ref. 27. Overall, our simulations reproduce the key features of the experimental energy-loss channel. In particular, all curves correctly show that the minimum energy loss corresponds to the gap energy. Some deviations remain: at $E_{in} = 0.99$ eV, the simulation overestimates the high energy-loss intensity due to contributions from low-energy distribution near $E \to 0$. This effect diminishes at higher incident energies as these components become less significant. At $E_{in} = 1.92$ eV, the simulated distribution nearly coincides with the experiment. For $E_{in} = 6.17$ eV, the results slightly overestimate the low-energy-loss intensity, whereas beyond the peak the distribution closely matches the experimental data. These deviations may reflect limitations of our model PES and parameters, yet the overall agreement demonstrates that our simulations capture the essential mechanisms of the energy-loss process.

Since nearly all of the scattered wavepacket populates the energy-loss channel for $\eta = 3$ eV, we further speculate that the two channels observed experimentally originate from collisions at different surface sites. Specifically, collisions of H with the surface rest atoms predominantly result in scattering through the energy-loss channel, while the elastic scattering channel mainly arises from collisions with other surface sites. Furthermore, the experimentally observed dependence of the branching ratio on E_{in} likely reflects the fact that changing the incident energy alters the relative probabilities of collisions at different surface sites. This finding provides direct support for the proposed site-specific scattering mechanism.[29,30]

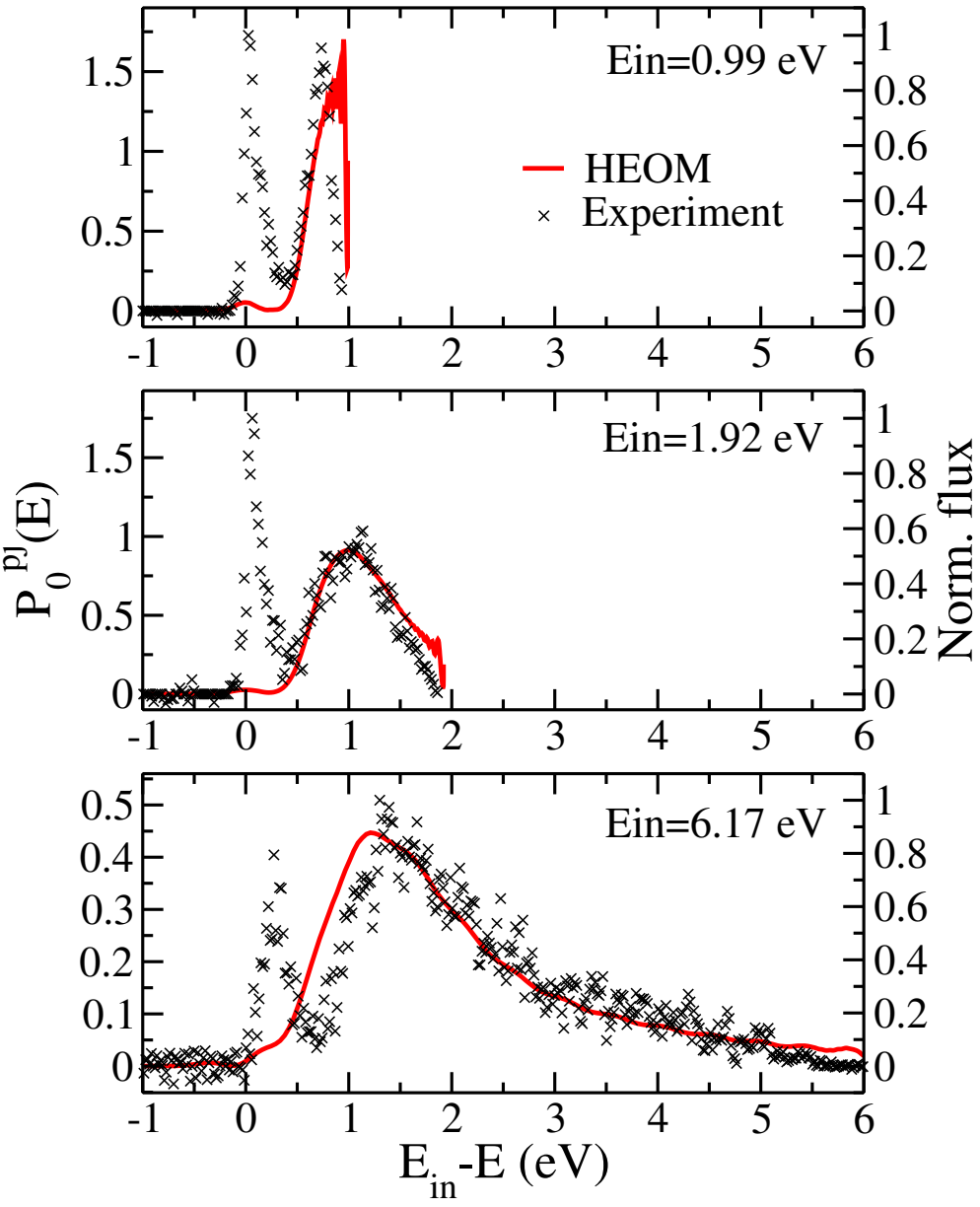

FIG. 10. Translational energy-loss distributions for different incident energies. HEOM simulations ($\eta = 3$ eV, from Figure 8; left y-axis) are plotted as a function of energy loss and compared with experimental data (normalized flux, right y-axis) from Fig. 1 of Ref. 27.

B. Isotope Effects: Simulation and Experiment

Recently, isotope effect measurements[29] show that for the adiabatic channel (or elastic scattering channel in this work), deuterium exhibits a larger energy loss than H, whereas the energy loss channel shows almost no isotope effect. Our simulation results do not capture the broadening of the elastic peak with increasing atomic mass. But it is noted that the

elastic channel is not our main focus, as it can already be reliably described by adiabatic MD simulations. Moreover, the Newns–Anderson model used here does not include coupling to surface phonons and is therefore not intended to reproduce adiabatic dynamics involving phonon interactions quantitatively.

For the more relevant energy-loss channel, which is strongly influenced by atom–surface interactions and directly linked to surface electronic properties, our simulations offer complementary insights and reveal new aspects of isotope effects. Although the experiment reports "almost no isotope effect" in this channel, a closer inspection of the energy-loss spectra (Fig. 2 of Ref. 29) reveals a slight but systematic difference between the H and D energy-loss peaks, with the D peak shifted toward smaller energy loss. This subtle trend is fully consistent with our prediction in Figure 9: increasing the atomic mass produces an effect analogous to a slight increase in the atom–surface coupling strength, shifting the deuterium peak toward higher energies (i.e., smaller energy loss). The weaker isotope effect observed experimentally likely arises from the statistical averaging over all surface sites, which diminishes the features associated with the rest site.

VI. CONCLUSIONS

We have employed the numerically exact hierarchical equations of motion (HEOM) method to simulate H-atom scattering from the Ge(111) surface. The one-dimensional PES for the H atom colliding with the rest site of Ge(111) was obtained from DFT calculations and fitted to the Newns–Anderson model to determine the model parameters. The simulations reveal two distinct scattering channels: an elastic channel without electron transfer and an energy-loss channel involving electron–hole excitations across the semiconductor band gap. These two channels produce a bimodal kinetic energy distribution of the scattered H atom, with peak separation consistent with the band gap.

Systematic variations of the atom–surface coupling strength, incident energy, and isotope substitution reveal clear mechanistic insights. Increasing the coupling strength drives scattering predominantly into the energy-loss channel, reduces both the energy loss and the broadening of the outgoing kinetic energy distribution, and enhances the adiabaticity of the dynamics. Higher incident energies promote the energy-loss channel, generating the bimodal structure. Isotope substitution (H $\rightarrow$ D) produces a similar impact as increasing

the atom–surface coupling strength.

Importantly, under strong atom–surface coupling, the overall shape and peak position of the simulated energy-loss peak closely match experimental observations while providing additional microscopic insight. HEOM captures high-energy electron–hole excitations in the energy-loss channel that cannot be described by electronic friction theory and other perturbative approaches,[27] addressing a key limitation of existing BOA-based methods. However, under this strong coupling, the elastic scattering channel is underestimated, supporting the experimentally proposed site-specific scattering mechanism, in which elastic scattering from other sites also contributes. Furthermore, while the experimental energy-loss peak appears relatively insensitive to isotope substitution, our results reveal a systematic shift of the deuterium peak toward smaller energy loss, highlighting the ability of HEOM simulations to uncover subtle quantum effects masked in ensemble-averaged measurements.

The fully quantum HEOM approach thus provides a benchmark for understanding H–semiconductor scattering at a fundamental level. Due to the substantial computational cost, we have employed a simplified Newns–Anderson model. Extending these simulations to fully realistic surface environments will require the development of efficient approximate methods.

Nonetheless, our fully quantum results offer valuable mechanistic insights and guidance for future modeling. As demonstrated, realistic scattering conditions correspond to a strong atom–surface coupling regime characterized by relatively adiabatic dynamics, albeit with characteristic band-gap-controlled energy loss. Incorporating such band-gap effects into extensions of electronic friction theory and related frameworks represents a promising avenue for future research.

ACKNOWLEDGMENTS

V. S. B. acknowledges support from the U.S. Army Research Office under Award W911NF-21-1-0337. X. D. thanks Dr. L. Zhu for helpful discussions regarding the computational results reported in their work, and Dr. O. Bünermann for kindly sharing the experimental data, and the Yale Center for Research Computing for a generous allocation of HPC time. Q. S. acknowledges support from the National Natural Science Foundation of China (Grant No. 22433006).

AVAILABILITY OF DATA

The data that support the findings of this study are available from the corresponding author upon reasonable request.

Parameter	Value
η	$1-3$ eV (varied)
ϵ_0	0.0 eV
γ	1.5 eV
E_B	0.49 eV
δ	0.02 eV
μ	0.0 eV
M	1836.013 au
T	300 K
A_0	0.19 eV
C_0	1.2 au
x_0	-3.8 au
A_1	11.81 eV
B_1	8.8 eV
C_1	0.32 au
D_1	0.94 au
x_1	-0.898 au
c_g	1.1 au
x_g	-2.8 au

TABLE I. Model parameters for the Newns-Anderson model.

REFERENCES

[1]M. Born and R. Oppenheimer, "Quantum theory of molecules," Annalen Der Physik **84**, 0457–0484 (1927).

[2]W. Domcke, D. Yarkony, and H. Köppel, *Conical Intersections: Electronic Structure, Dynamics and Spectroscopy* (World Scientific, Singapore, 2004).

[3]M. S. Schuurman and A. Stolow, "Dynamics at conical intersections," Annu. Rev. Phys. Chem. **69**, 427–450 (2018).

[4]G. Li, B. Movaghar, A. Nitzan, and M. A. Ratner, "Polaron formation: Ehrenfest dynamics vs. exact results," J. Chem. Phys. **138**, 044112 (2013), https://pubs.aip.org/aip/jcp/article-pdf/doi/10.1063/1.4776230/15459153/044112_1_online.pdf.

[5]L. Chen, Y. Zhao, and Y. Tanimura, "Dynamics of a one-dimensional holstein polaron with the hierarchical equations of motion approach," J. Phys. Chem. Lett. **6**, 3110 (2015).

[6]C. Franchini, M. Reticcioli, M. Setvin, and U. Diebold, "Polarons in materials," Nat. Rev. Mater. **6**, 560–586 (2021).

[7]X. Sun, P. Zhang, Y. Lai, K. L. Williams, M. S. Cheung, B. D. Dunietz, and E. Geva, "Computational study of charge-transfer dynamics in the carotenoid–porphyrin–c60 molecular triad solvated in explicit tetrahydrofuran and its spectroscopic signature," J. Phys. Chem. C **122**, 11288–11299 (2018).

[8]Z. Tong, X. Gao, M. S. Cheung, B. D. Dunietz, E. Geva, and X. Sun, "Charge transfer rate constants for the carotenoid-porphyrin-C60 molecular triad dissolved in tetrahydrofuran: The spin-boson model vs the linearized semiclassical approximation," J. Chem. Phys. **153**, 044105 (2020).

[9]G. S. Engel, T. R. Calhoun, E. L. Read, T.-K. Ahn, T. Mancal, Y.-C. Cheng, R. E. Blankenship, and G. R. Fleming, "Evidence for wavelike energy transfer through quantum coherence in photosynthetic systems," Nature **446**, 782–786 (2007).

[10]A. Ishizaki and G. R. Fleming, "Theoretical examination of quantum coherence in a photosynthetic system at physiological temperature," Proc. Natl. Acad. Sci. USA **106**, 17255 (2009).

[11]G. D. Scholes, G. R. Fleming, L. X. Chen, A. Aspuru-Guzik, A. Buchleitner, D. F. Coker, G. S. Engel, R. van Grondelle, A. Ishizaki, D. M. Jonas, J. S. Lundeen, J. K. McCusker, S. Mukamel, J. P. Ogilvie, A. Olaya-Castro, M. A. Ratner, F. C. Spano, K. B. Whaley, and X. Zhu, "Using coherence to enhance function in chemical and biophysical systems," Nature **543**, 647–656 (2017).

[12]X. Dan, E. Geva, and V. S. Batista, "Simulating non-markovian quantum dynamics on nisq computers using the hierarchical equations of motion," J. Chem. Theory Comput. **21**, 1530–1546 (2025), https://doi.org/10.1021/acs.jctc.4c01565.

[13]A. M. Wodtke, "Electronically non-adiabatic influences in surface chemistry and dynamics," Chem. Soc. Rev. **45**, 3641–3657 (2016).

[14]A. Kandratsenka, H. Jiang, Y. Dorenkamp, S. M. Janke, M. Kammler, A. M. Wodtke, and O. Bünermann, "Unified description of H-atom–induced chemicurrents and inelastic scattering," Proc. Natl. Acad. Sci. USA **115**, 680–684 (2018).

[15]O. Bünermann, H. Jiang, Y. Dorenkamp, A. Kandratsenka, S. M. Janke, D. J. Auerbach, and A. M. Wodtke, "Electron–hole pair excitation determines the mechanism of hydrogen atom adsorption," Science **350**, 1346–1349 (2015).

[16]Y. Dorenkamp, H. Jiang, H. Köckert, N. Hertl, M. Kammler, S. M. Janke, A. Kandratsenka, A. M. Wodtke, and O. Bünermann, "Hydrogen collisions with transition metal surfaces: Universal electronically nonadiabatic adsorption," J. Chem. Phys. **148**, 034706 (2018).

[17]M. Alducin, R. Díez Muiño, and J. Juaristi, "Non-adiabatic effects in elementary reaction processes at metal surfaces," Prog. Surf. Sci. **92**, 317–340 (2017).

[18]M. Head-Gordon and J. C. Tully, "Molecular dynamics with electronic frictions," J. Chem. Phys. **103**, 10137–10145 (1995).

[19]V. Krishna and J. C. Tully, "Vibrational lifetimes of molecular adsorbates on metal surfaces," J. Chem. Phys. **125**, 054706 (2006).

[20]W. Dou and J. E. Subotnik, "Perspective: How to understand electronic friction," J. Chem. Phys. **148**, 230901 (2018).

[21]R. J. Maurer, M. Askerka, V. S. Batista, and J. C. Tully, "Ab initio tensorial electronic friction for molecules on metal surfaces: Nonadiabatic vibrational relaxation," Phys. Rev. B **94**, 115432 (2016).

[22]P. Spiering and J. Meyer, "Testing electronic friction models: vibrational de-excitation in scattering of H2 and D2 from Cu(111)," J. Phys. Chem. Lett. **9**, 1803–1808 (2018), pMID: 29528648.

[23]R. Martin-Barrios, N. Hertl, O. Galparsoro, A. Kandratsenka, A. M. Wodtke, and P. Larrégaray, "H atom scattering from W(110): A benchmark for molecular dynamics with electronic friction." Phys. Chem. Chem. Phys. **24**, 20813–20819 (2022).

[24]Y. Li and G. Wahnström, "Molecular-dynamics simulation of hydrogen diffusion in palladium," Phys. Rev. B **46**, 14528–14542 (1992).

[25]C. L. Box, Y. Zhang, R. Yin, B. Jiang, and R. J. Maurer, "Determining the effect of hot electron dissipation on molecular scattering experiments at metal surfaces," JACS Au **1**, 164–173 (2021), https://doi.org/10.1021/jacsau.0c00066.

[26]J. Gardner, S. Habershon, and R. J. Maurer, "Assessing mixed quantum-classical molecular dynamics methods for nonadiabatic dynamics of molecules on metal surfaces," J. Phys. Chem. C **127**, 15257–15270 (2023), https://doi.org/10.1021/acs.jpcc.3c03591.

[27]K. Krüger, Y. Wang, S. Tödter, F. Debbeler, A. Matveenko, N. Hertl, X. Zhou, B. Jiang, H. Guo, A. M. Wodtke, *et al.*, "Hydrogen atom collisions with a semiconductor efficiently promote electrons to the conduction band," Nat. Chem. **15**, 326–331 (2023).

[28]S. Malpathak and N. Ananth, "A linearized semiclassical dynamics study of the multiquantum vibrational relaxation of no scattering from a au(111) surface," J. Phys. Chem. Lett. **15**, 794–801 (2024), pMID: 38232133, https://doi.org/10.1021/acs.jpclett.3c03041.

[29]K. Krüger, Y. Wang, L. Zhu, B. Jiang, H. Guo, A. M. Wodtke, and O. Bünermann, "Isotope effect suggests site-specific nonadiabaticity on ge(111)c(2×8)," Nat. Sci. **4**, e20230019 (2024), https://onlinelibrary.wiley.com/doi/pdf/10.1002/ntls.20230019.

[30]L. Zhu, Q. Zheng, Y. Wang, K. Krüger, A. M. Wodtke, O. Bünermann, J. Zhao, H. Guo, and B. Jiang, "Mechanistic insights into nonadiabatic interband transitions on a semiconductor surface induced by hydrogen atom collisions," JACS Au **4**, 4518–4526 (2024).

[31]X. Lu, N. Hertl, and R. J. Maurer, "A haldane-anderson hamiltonian model for hyperthermal hydrogen scattering from a semiconductor surface," (2025), arXiv:2508.13360.

[32]Y. Tanimura and R. Kubo, "Time evolution of a quantum system in contact with a nearly gaussian-markoffian noise bath," J. Phys. Soc. Jpn. **58**, 101–114 (1989).

[33]Y. Tanimura, "Stochastic liouville, langevin, fokker–planck, and master equation approaches to quantum dissipative systems," J. Phys. Soc. Jpn. **75**, 082001 (2006).

[34]J. Jin, S. Welack, J. Luo, X.-Q. Li, P. Cui, R.-X. Xu, and Y. Yan, "Dynamics of quantum dissipation systems interacting with fermion and boson grand canonical bath ensembles: Hierarchical equations of motion approach," J. Chem. Phys. **126**, 134113 (2007).

[35]J. Jin, X. Zheng, and Y. Yan, "Exact dynamics of dissipative electronic systems and quantum transport: Hierarchical equations of motion approach," J. Chem. Phys. **128**, 234703 (2008).

[36]R. Härtle, G. Cohen, D. Reichman, and A. Millis, "Transport through an Anderson impurity: Current ringing, nonlinear magnetization, and a direct comparison of continuous-time quantum Monte Carlo and hierarchical quantum master equations," Phys. Rev. B **92**, 085430 (2015).

[37]C. Schinabeck, A. Erpenbeck, R. Härtle, and M. Thoss, "Hierarchical quantum master equation approach to electronic-vibrational coupling in nonequilibrium transport through nanosystems," Phys. Rev. B **94**, 201407 (2016).

[38]A. Erpenbeck, L. Götzendörfer, C. Schinabeck, and M. Thoss, "Hierarchical quantum master equation approach to charge transport in molecular junctions with time-dependent molecule-lead coupling strengths," Eur. Phys. J.-Spec. Top. **227**, 1981–1994 (2019).

[39]A. Erpenbeck, Y. Ke, U. Peskin, and M. Thoss, "Current-induced dissociation in molecular junctions beyond the paradigm of vibrational heating: The role of antibonding electronic states," Phys. Rev. B **102**, 195421 (2020).

[40]H.-D. Zhang, L. Cui, H. Gong, R.-X. Xu, X. Zheng, and Y. Yan, "Hierarchical equations of motion method based on fano spectrum decomposition for low temperature environments," J. Chem. Phys. **152**, 064107 (2020).

[41]Y. Ke, A. Erpenbeck, U. Peskin, and M. Thoss, "Unraveling current-induced dissociation mechanisms in single-molecule junctions," J. Chem. Phys. **154**, 234702 (2021).

[42]C. Kaspar, A. Erpenbeck, J. Bätge, C. Schinabeck, and M. Thoss, "Nonadiabatic vibronic effects in single-molecule junctions: A theoretical study using the hierarchical equations of motion approach," Phys. Rev. B **105**, 195435 (2022).

[43]R. J. Preston, Y. Ke, S. L. Rudge, N. Hertl, R. Borrelli, R. J. Maurer, and M. Thoss, "Nonadiabatic quantum dynamics of molecules scattering from metal surfaces," Journal of Chemical Theory and Computation **21**, 1054–1063 (2025).

[44]Q. Shi, Y. Xu, Y. Yan, and M. Xu, "Efficient propagation of the hierarchical equations of motion using the matrix product state method," J. Chem. Phys. **148**, 174102 (2018).

[45]Y. Ke, R. Borrelli, and M. Thoss, "Hierarchical equations of motion approach to hybrid fermionic and bosonic environments: Matrix product state formulation in twin space," J. Chem. Phys. **156**, 194102 (2022).

[46]W. Guan, P. Bao, J. Peng, Z. Lan, and Q. Shi, "mpsqd: A matrix product state based python package to simulate closed and open system quantum dynamics," J. Chem. Phys. **161**, 122501 (2024), https://pubs.aip.org/aip/jcp/article-pdf/doi/10.1063/5.0226214/20174778/122501_1_5.0226214.pdf.

[47]S. Zhang, Z. Liu, P. Bao, and Q. Shi, "A multiset matrix product state approach to hierarchical equations of motion and its application to vibrational relaxation on metal surfaces," J. Chem. Phys. **163**, 094102 (2025).

[48]M. Xu, Y. Yan, Q. Shi, J. Ankerhold, and J. T. Stockburger, "Taming quantum noise for efficient low temperature simulations of open quantum systems," Phys. Rev. Lett. **129**, 230601 (2022).

[49]X. Dan, M. Xu, J. T. Stockburger, J. Ankerhold, and Q. Shi, "Efficient low-temperature simulations for fermionic reservoirs with the hierarchical equations of motion method: Application to the Anderson impurity model," Phys. Rev. B **107**, 195429 (2023).

[50]Y. Nakatsukasa, O. Sète, and L. N. Trefethen, "The aaa algorithm for rational approximation," SIAM J SCI COMPUT **40**, A1494–A1522 (2018).

[51]C. Hofreither, "An algorithm for best rational approximation based on barycentric rational interpolation," Numer Algorithms **88**, 365–388 (2021).

[52]H. Takahashi, S. Rudge, C. Kaspar, M. Thoss, and R. Borrelli, "High accuracy exponential decomposition of bath correlation functions for arbitrary and structured spectral densities: Emerging methodologies and new approaches," J. Chem. Phys. **160**, 204105 (2024), https://pubs.aip.org/aip/jcp/article-pdf/doi/10.1063/5.0209348/19961639/204105_1_5.0209348.pdf.

[53]P. W. Anderson, "Localized magnetic states in metals," Phys. Rev. **124**, 41–53 (1961).

[54]D. M. Newns, "Self-consistent model of hydrogen chemisorption," Phys. Rev. **178**, 1123–1135 (1969).

[55]W. Schmickler, "A theory of adiabatic electron-transfer reactions," J. Electroanal. Chem. Interfac. **204**, 31–43 (1986).

[56]W. Schmickler and J. Mohr, "The rate of electrochemical electron-transfer reactions," J. Chem. Phys. **117**, 2867–2872 (2002).

[57]A. Nitzan, "Electron transmission through molecules and molecular interfaces," Annu. Rev. Phys. Chem. **52**, 681–750 (2001).

[58]W. Dou and J. E. Subotnik, "Electronic friction near metal surfaces: A case where molecule-metal couplings depend on nuclear coordinates," J. Chem. Phys. **146**, 092304 (2017).

[59]T. Klitsner and J. S. Nelson, "Site-specific hydrogen reactivity and reverse charge transfer on ge(111)-c(2×8)," Phys. Rev. Lett. **67**, 3800–3803 (1991).

[60]I. Razado, H. Zhang, G. Hansson, and R. Uhrberg, "Hydrogen-induced metallization on ge(111) c(2×8)," Appl. Surf. Sci. **252**, 5300–5303 (2006).

[61]X. Dan and Q. Shi, "Theoretical study of nonadiabatic hydrogen atom scattering dynamics on metal surfaces using the hierarchical equations of motion method," J. Chem. Phys. **159**, 044101 (2023).

[62]G. D. Mahan, *Many-Particle Physics* (Kluwer Academic/Plenum, New York, 2000).

[63]H. Haug, A.-P. Jauho, *et al.*, *Quantum kinetics in transport and optics of semiconductors*, Vol. 2 (Springer, 2008).

[64]X. Dan, M. Xu, Y. Yan, and Q. Shi, "Generalized master equation for charge transport in a molecular junction: Exact memory kernels and their high order expansion," J. Chem. Phys. **156**, 134114 (2022).

[65]J. Muscat and D. Newns, "Chemisorption on metals," Prog. Surf. Sci. **9**, 1–43 (1978).

[66]R. Härtle, G. Cohen, D. R. Reichman, and A. J. Millis, "Decoherence and lead-induced interdot coupling in nonequilibrium electron transport through interacting quantum dots: A hierarchical quantum master equation approach," Phys. Rev. B **88**, 235426 (2013).

[67]M. Xu, Y.-Y. Liu, K. Song, and Q. Shi, "A non-perturbative approach to simulate heterogeneous electron transfer dynamics: Effective mode treatment of the continuum electronic states," J. Chem. Phys. **150**, 044109 (2019).

[68]A. Erpenbeck, C. Schinabeck, U. Peskin, and M. Thoss, "Current-induced bond rupture in single-molecule junctions," Phys. Rev. B **97**, 235452 (2018).

[69]C. Lubich, I. Oseledets, and B. Vandereycken, "Time integration of tensor trains," SIAM J. Numer. Anal. **53**, 917–941 (2015).

[70]P. E. Blöchl, "Projector augmented-wave method," Phys. Rev. B **50**, 17953–17979 (1994).

[71]J. P. Perdew, K. Burke, and M. Ernzerhof, "Generalized gradient approximation made simple," Phys. Rev. Lett. **77**, 3865–3868 (1996).

[72]S. Grimme, J. Antony, S. Ehrlich, and H. Krieg, "A consistent and accurate ab initio parametrization of density functional dispersion correction (dft-d) for the 94 elements h-pu," J. Chem. Phys. **132**, 154104 (2010).

[73]S. Grimme, S. Ehrlich, and L. Goerigk, "Effect of the damping function in dispersion corrected density functional theory," J. Comput. Chem. **32**, 1456–1465 (2011).

[74]H. J. Monkhorst and J. D. Pack, "Special points for brillouin-zone integrations," Phys. Rev. B **13**, 5188–5192 (1976).

[75]D. J. Chadi and C. Chiang, "New $c-2\times 8$ unit cell for the ge(111) surface," Phys. Rev. B **23**, 1843–1846 (1981).

[76]G. Gobeli and F. Allen, "Photoelectric properties and work function of cleaved germanium surfaces," Surface Science **2**, 402–408 (1964).

[77]J. Echave and D. C. Clary, "Potential optimized discrete variable representation," Chem. Phys. Lett. **190**, 225–230 (1992).

[78]D. T. Colbert and W. H. Miller, "A novel discrete variable representation (dvr) for quantum mechanical reactive scattering via the s-matrix kohn method," J. Chem. Phys. **96**, 1982–1991 (1992).

[79]L. Landau, "On the theory of transfer of energy at collisions ii," Physik. Z. Sow. **2**, 46 (1932).

[80]C. Zener, "Non-adiabatic crossing of energy levels," Proc. R. Soc. London Ser. A **137**, 696–702 (1932).

[81]A. Nitzan, *Chemical Dynamics in Condensed Phases* (Oxford University Press, New York, 2006).